Contents lists available at ScienceDirect

Applied Geochemistry
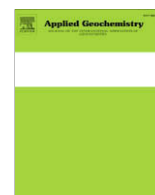
Characterization of manganese oxide precipitates from Appalachian coal mine drainage treatment systems

Hui Tan[a], Gengxin Zhang[a], Peter J. Heaney[b], Samuel M. Webb[c], William D. Burgos[a,*]

[a] Department of Civil and Environmental Engineering, The Pennsylvania State University, 212 Sackett Building, University Park, PA 16802, USA
[b] Department of Geosciences, The Pennsylvania State University, University Park, PA, USA
[c] Stanford Synchrotron Radiation Laboratory, Menlo Park, CA, USA

ARTICLE INFO

ABSTRACT

The removal of Mn(II) from coal mine drainage (CMD) by chemical addition/active treatment can significantly increase treatment costs. Passive treatment for Mn removal involves promotion of biological oxidative precipitation of manganese oxides (MnO_x). Manganese(II) removal was studied in three passive treatment systems in western Pennsylvania that differed based on their influent Mn(II) concentrations (20–150 mg/L), system construction (±inoculation with patented Mn(II)-oxidizing bacteria), and bed materials (limestone vs. sandstone). Manganese(II) removal occurred at pH values as low as 5.0 and temperatures as low as 2 °C, but was enhanced at circumneutral pH and warmer temperatures. Trace metals such as Zn, Ni and Co were removed effectively, in most cases preferentially, into the MnO_x precipitates. Based on synchrotron radiation X-ray diffraction and Mn K-edge extended X-ray absorption fine structure spectroscopy, the predominant Mn oxides at all sites were poorly crystalline hexagonal birnessite, triclinic birnessite and todorokite. The surface morphology of the MnO_x precipitates from all sites was coarse and "sponge-like" composed of nm-sized lathes and thin sheets. Based on scanning electron microscopy (SEM), MnO_x precipitates were found in close proximity to both prokaryotic and eukaryotic organisms. The greatest removal efficiency of Mn(II) occurred at the one site with a higher pH in the bed and a higher influent total organic C (TOC) concentration (provided by an upstream wetland). Biological oxidation of Mn(II) driven by heterotrophic activity was most likely the predominant Mn removal mechanism in these systems. Influent water chemistry and Mn(II) oxidation kinetics affected the relative distribution of MnO_x mineral assemblages in CMD treatment systems.

© 2009 Elsevier Ltd. All rights reserved.

1. Introduction

The removal of Mn(II) from coal mine drainage (CMD) is a significant problem for both operating and abandoned coal mines in Pennsylvania and across the USA. Manganese(II)-elevated mine drainage exists in all eastern USA coal producing states. According to the US Office of Surface Mining (OSM) mine drainage inventory, Mn(II) is being treated at more than 700 mine sites in Appalachia (60% of sites) and most coal operators use NaOH to remove Mn(II) from mine drainage. Sodium hydroxide is added to raise the pH to ~9–10 to promote the abiotic oxidation of soluble Mn(II) to insoluble Mn(III/IV) (oxyhydr)oxides (referred to hereafter as "MnO_x"). Active Mn(II) removal (i.e. NaOH addition) can double or triple treatment costs due to the chemical consumption needed to achieve high pH conditions (Means and Hilton, 2004). Passive removal of Mn(II) is desirable as it eliminates the need for chemical reagent and the annual treatment costs can be a small fraction compared to active treatment. The success of passive Mn(II) removal systems has been variable due to a lack of design criteria and a poor understanding of the mechanisms that govern Mn(II) oxidation at circumneutral pH.

Passive limestone beds neutralize acidic water and promote biologically-mediated Mn(II) oxidation (Thornton, 1995; Sikora et al., 2000; Vail and Riley, 2000; Johnson and Younger, 2005; Means and Rose, 2005). Widespread and diverse bacteria, fungi, and algae are capable of coupling the enzymatic oxidation of Mn(II) (and subsequent precipitation of MnO_x) to O_2 reduction at circumneutral pH (Ghiorse, 1984; Tebo et al., 2004; Thompson et al., 2005; Templeton et al., 2005; Hansel and Francis, 2006). Biological Mn(II) oxidation has been exploited to remove Mn(II) from drinking water in sand filtration systems inoculated with Mn(II)-oxidizing bacteria (Mouchet, 1992; Katsoyiannis et al., 2004). In CMD limestone beds, Mn(II) is removed and accumulates in these systems as MnO_x coatings that can in turn catalyze additional Mn(II) removal. Wetlands are often placed upstream of limestone beds

to provide organic C and nutrients for indigenous or inoculated Mn(II)-oxidizing bacteria (Mn(II)OB) (Thornton, 1995; Vail and Riley, 2000; Johnson and Younger, 2005).

At circumneutral pH, Mn(II) may be oxidized by microbiological activity or by surface-catalyzed heterogeneous oxidation on Mn(III/IV) oxide surfaces (Davies and Morgan, 1989; Junta and Hochella, 1994). Currently, the relative importance of biological Mn(II) oxidation vs. abiotic surface-catalyzed Mn(II) oxidation in these systems is uncertain (Means and Rose, 2005). However, much of the Mn(II) oxidation observed in natural systems is believed to be biologically-mediated (Hungate et al., 1987; Nealson et al., 1988; Tebo, 1991; Tebo et al., 1997).

The mechanism for biogenic MnO_x formation has been developed from pure bacterial culture studies coupled with X-ray absorption spectroscopy (XAS) and synchrotron radiation X-ray diffraction (SR-XRD) (Bargar et al., 2000, 2005: Villalobos et al., 2003; Webb et al., 2005a). Bacteria use O_2 and a Mn-oxidase enzyme to oxidize Mn^{2+} to Mn^{4+} (likely through Mn^{3+}) and Mn^{4+} rapidly hydrolyzes to form disordered nanoparticulate (DN) MnO_2. DN MnO_2 then forms small, poorly crystalline Ca-hexagonal birnessite, and finally transitions into Ca-pseudo-orthogonal birnessite (Webb et al., 2005a). While this mechanism has been worked out in fine detail with model biological systems, subsequent mineralogical transformations are critical in controlling the MnO_x mineral(s) found in a particular environment. The stability and predominance of the over 30 MnO_x minerals are strongly dependent on solution chemistry (e.g. freshwater vs. seawater). Calcium in particular is hypothesized to stabilize and promote the growth of biogenic birnessites (Webb et al., 2005b). However, MnO_x minerals are also quite labile and respond to thermodynamic driving forces such that rapid conversion between mineral phases can occur (Bargar et al., 2005; Lopano et al., 2007).

Manganese oxides exert significant control on the distribution of trace metals in soils and aquatic environments because of their high adsorption capacities (Post, 1999). Often occurring as fine grained particles and surface coatings, MnO_x provide large reactive surface areas far more than their proportional concentrations (Jenne, 1968). Several studies have demonstrated that MnO_x can serve as natural sinks for Co, Ni, Zn and other metals in mine tailing sites and streams impacted by mining activities (Fuller and Harvey, 2000; Kay et al., 2001; Tani et al., 2004). MnO_x also participate in a wide range of redox reactions, including oxidation of As(III) to As(V), Cr(III) to Cr(VI), and degradation of organic contaminants (PCBs, phenols and chlorinated solvents) (Manceau and Charlet, 1992; Stone, 1987).

Regardless of the abiotic or microbial oxidation pathway and the subsequent stabilization of the MnO_x, the mineralogical and physicochemical properties of the MnO_x formed in CMD treatment systems (or in any other environment) will directly affect their ability to remove additional Mn(II) and other metal co-contaminants. In this study the performance of three passive Mn-removal systems in western Pennsylvania has been monitored and the MnO_x formed in these beds characterized by electron microscopy, XRD and XAS. The objective was to evaluate how aqueous geochemical conditions and MnO_x properties may contribute to the enhanced removal of Mn(II) and associated trace metals.

2. Materials and methods

2.1. Site descriptions

Personnel from the OSM directed the authors to three Mn-removal systems located in western Pennsylvania that differed based on their influent Mn(II) concentrations (20–150 mg/L), system construction (±inoculation with patented Mn(II)OB), and bed materials

(limestone vs. sandstone). All of the systems are treating CMD from surface coal mines. Important physical, chemical and operational features of these treatment systems are presented in Table 1.

The treatment system at Site 1 was filled with limestone gravel (4 in.), was not inoculated with Mn(II)OB, and treats an exceptionally high influent Mn(II) concentration of 130–150 mg/L. CMD is conveyed through an underground limestone drain before discharging into a constructed wetland and then enters the limestone Mn-removal bed. Discharge into the wetland comes from a pipe elevated several feet above the ground that provides aeration as the water enters the wetland. The rectangular bed contains five ditches (perpendicular to bed flow, ~½ the depth of the bed) that were added to promote passive aeration and served as the water and sediment sampling locations.

The treatment system at Site 2 was filled with limestone gravel (1 in.) and inoculated with a patented suspension of Mn(II)OB (Pyrolusite Process®; Vail and Riley, 2000), and treats an influent Mn(II) concentration of 20–30 mg/L. CMD flows into a constructed wetland, then into the limestone bed, and is aerated before the limestone bed by discharge through an elevated pipe. The narrow rectangular bed contained three piezometers that were used to collect water samples within the bed.

The treatment system at Site 3 includes three ponds in series designed to remove both Fe (in the first two ponds) and Mn (in the final pond) from a circumneutral-pH surface coal mine discharge. In the final pond, a 2-m wide sandstone barrier was constructed across the pond (perpendicular to bed flow and breaching the water surface) to serve as a reactive surface for MnO_x precipitation. Sandstone was used because of its lower local cost compared to limestone and because the discharge already had a circumneutral pH.

2.2. Sample collection and preparation

Field measurements included influent flow rate (bucket and stopwatch), and electrical conductivity (conductivity cell), dissolved O_2 (galvanic probe), and pH and temperature (combination electrode) using portable meters. Water samples were filtered (0.2-μm) into pre-cleaned centrifuge tubes (pre-washed with 10% HNO_3) and chemically preserved in the field with HNO_3 (for metal analysis) or H_2SO_4 (for total organic C analysis). Water samples were transported to the laboratory on ice and refrigerated at 4 °C until analyzed. At Site 1, samples were collected from the influent pipe and the center of each ditch. At Site 2, samples were collected from the influent pipe, several test pits dug into the bed, three piezometers within the bed, and the effluent stream. At Site 3, samples were collected from the pipe into the final pond and from upstream and downstream of the sandstone barrier. Sediment "crust" samples were collected from the top 1-cm of precipitates found in the ditches at Site 1, in the influent surface ditch, test pits and the effluent stream at Site 2, and on the sandstone barrier at Site 3. Sediment samples were collected with sterile spatulas and placed in sterile centrifuge tubes or whirl-paks. All sediment samples were stored on ice for transport to the laboratory. Wet sediments were passed through a 2-mm sieve and the <2-mm sieve fractions were homogenized and used for all solid-phase analyses. Visually these sieve fractions contained mixtures of MnO_x, quartz, and limestone or sandstone fragments.

2.3. Chemical analyses

Water samples were analyzed for dissolved metals, anions, alkalinity, hot-peroxide acidity, total organic C (TOC), and total organic N (TON). Cations (Al, Ba, Ca, Fe, K, Mg, Mn, Na, Si, Sr, Ti, Co, Ni, Zn) were measured using a Leeman Labs PS3000UV inductively coupled plasma atomic emission spectrophotometer (ICP-AES).

Table 1
Physical characteristics of the three Mn-removal treatment systems.

	Site 1	Site 2	Site 3
Geographic coordinates	41°2′105″N 78°39′16″W	40°03′01″N 78°48′39″W	41°18′49″N 78°44′23″W
Year constructed	2004	1998	2007
Size: $L \times W \times D$ (m)	$30 \times 15 \times 1$	$70 \times 7 \times 1$	See text
Flow rate (L s^{-1})	0.63	0.63	0.32
Hydraulic residence Time (h)[a]	100	110	n/d
Substrate	Limestone AASHTO #56 ~10 cm (4 in.) dia	Limestone AASHTO #3 ~2.5 cm (1 in.) dia	Sandstone 10 cm (4 in.) dia[b]
Mn(II)OB inocula	None	Yes[c]	None
Organic substrate	Straw and corn cobs	None	None
Upstream wetland	Yes	Yes	None

[a] Hydraulic residence times were calculated assuming a bed porosity of 0.5 or not determined (n/d).
[b] The system is not filled with sandstone, but a sandstone ridge (2 m wide) was constructed across the pond perpendicular to the general flow direction.
[c] Pyrolusite process (Vail and Riley, 2000).

Manganese(II) concentrations were determined by the pyridylazo-naphthol (PAN) method (Goto et al., 1977) and were found to be identical to the total Mn concentrations measured by ICP-AES. Anions (SO_4^{2-}, NO_3^-, NO_2^-, Cl^- and acetate) were measured using a Dionex DX-100 ion chromatograph. Alkalinity and hot-peroxide acidity were measured by standard volumetric titrations. TOC and TON were measured using a Shimadzu 5000A TOC/TON analyzer. Total P was analyzed by Hach PhosVer 3 with the Acid Persulfate Digestion Test 'N Tube Method 8190.

Elemental analysis of the sediments was performed by Li metaborate fusion followed by ICP-AES. Sediment samples were air-dried at room temperature for several days until the water content stabilized. Sediment samples were then heated to 750 °C overnight to remove organic matter. Each sample was then mixed with Li metaborate and heated to 900 °C in a graphite crucible for 10 min. The melted liquid was then quickly transferred into a Teflon beaker containing 5% HNO_3. The solution was stirred for 15 min and then analyzed by ICP-AES. Elemental sediment concentrations were reported in oxide form based on the dry sediment mass.

2.4. Electron microscopy

To preserve biological features in the sediments, samples were fixed in the field with 2.5% glutaraldehyde in 0.05 M Na cacodylate buffer at pH 7. One drop of the fixed sample was transferred onto the surface of a glass cover slip that had been washed with a polylysine solution prior to use. Mineral particles were allowed to settle onto the cover slip for 20 min. The particle-coated cover slips were gradually dehydrated in an ethanol series followed by critical point drying (31 °C and 74 bar). Cover slips were mounted on a SEM stub and Au-Pd coated for observation using a Zeiss Supra 35 FEG-VP SEM at an accelerating voltage of 10–15 kV. A short working distance (6–10 mm) and low beam current (30–40 mA) were used to achieve the best image resolution. A longer working distance (8.0 mm) and higher beam current (50–70 mA) were used for energy dispersive spectroscopy (EDS) analysis.

For whole mount transmission electron microscopy (TEM), sieved and air-dried sediment samples were dispersed into ethanol and sonicated for 15 min. A drop of the sonicated sample was placed on a 400 mesh C-sputtered formvar-coated Cu grid, air dried, and examined with a JEOL 2010 high resolution TEM with a LaB$_6$ filament operating at 200 kV. Elemental analysis was performed using an Oxford EDS system equipped with a SiLi detector coupled to the EM. Images and select area electron diffraction (SAED) patterns were recorded on films and later digitally scanned for further analysis.

2.5. X-ray diffraction

XRD patterns were collected on both wet and dry samples (oven-dried at 110 °C overnight). Samples were examined using a Rigaku Geigerflex microdiffractometer equipped with a graphite monochromater and a cylindrical image plate area detector. A Mo tube (50 kV, 40 mA) was used as the X-ray source and a 0.3 mm collimator was used to ensure parallel X-ray beams. Samples were packed into 0.7 mm diameter quartz capillaries (Charles Supper Co., Natick, MA) and mounted into a Cu sample holder. During exposure to the X-ray beam, the sample was oscillated between 2° and 10° omega angle and −30° to +30° phi angle simultaneously to minimize the effects of sample heterogeneity and preferred orientation.

Select samples were examined at the X7B beam line of the National Synchrotron Light Source (NSLS) at Brookhaven National Laboratory. Samples were packed into 1.0 mm diameter quartz capillaries and SR-XRD patterns were collected with a MAR 345 full imaging plate detector. During exposure to the X-ray beam, the samples were fully rotated through 360° during sample collection. The contribution of instrumental broadening to peak width was measured using a LaB$_6$ standard. Select samples were examined at the Stanford Synchrotron Radiation Laboratory (SSRL) on beam line 11–3 using a MAR 345 image plate detector. Analysis of all XRD patterns was performed using the JADE 6.5 software package.

2.6. X-ray absorption spectroscopy

Bulk Mn K-edge extended X-ray absorption fine structure (EXAFS) spectra from wet sediment coatings were measured in transmission mode at room temperature at SSRL beam line 11-2 (variable-exit Si(2 2 0) monochromator). Harmonic content in the X-ray beam was attenuated by use of a collimating mirror set at 11.5 keV and by detuning the monochromator. Samples were loaded into rigid thermoplastic sample holders with Lexan windows to maintain hydrated conditions. Energy calibration was monitored using the pre-edge peak of $KMnO_4$ (6543.34 eV). Beam dimension at the sample at beam line 11-2 was typically 5 mm (horizontal) $\times$ 0.5 mm (vertical), with a flux density of ca 1010 photons/s. Reduction of Mn(IV) oxides was not observed to occur at this flux density within the time scale of the measurements. Manganese K-edge EXAFS were stable over several hour exposures, indicating that the unfocused X-ray beam at beam line 11-2 did not damage the sample. Typically one or two EXAFS scans were measured on each sample (30–60 min). EXAFS spectra were background-subtracted, normalized, and analyzed in SIXPACK/

Table 2
Chemistry of influent water of the three treatment systems (in mg/L). Values presented as ranges reflect spatial variance within the systems and temporal variance over several seasons.

	Site 1	Site 2	Site 3
Alkalinity (mg CaCO$_3$/L)	28	5	92
Hot-peroxide acidity (mg CaCO$_3$/L)	373	110	19
pH	5.23	4.74	7.43
Total organic carbon (mg C/L) 1.0–13	8.9–28	2.5	
Total nitrogen (mg N/L)	0.07–0.46	0.13	n/a
Total phosphorous (mg P/L)	<0.01	<0.01	n/a
Mn	150	30	27
Fe	<0.05	0.62	0.11
Al	8.62	7.95	0.36
Ca	225–365	230–370	175
Mg	255	220	95
Si	6.5	5.8	3.3
Zn	0.685	0.919	0.011
Ni	0.591	0.641	0.091
Co	0.341	0.186	0.048
Cr	0.024	0.006	0.008
Pb	0.010	0.005	0.005
Cu	0.005	0.010	0.003
SO_4^{2-}	2010	992	498
Cl^-	2.4	14	0.64
NO_3^-	0.44	0.12	0.81

IFEFFIT. Phase and amplitude files for the EXAFS fitting were created with FEFF6 (Rehr et al., 1992). Manganese-EXAFS were fit using a model based on a phyllomanganate structure developed by Webb et al. (2005b). A linear combination fitting (LCF) of hexagonal birnessite, triclinic birnessite and todorokite was used to fit the sample Mn-EXAFS spectra.

3. Results and discussion

3.1. Water chemistry

In Appalachian coal mine drainage, Fe, Al and Mn are typically the most important metal contaminants with respect to elevated concentrations and treatment priorities. Manganese in CMD may originate from metal sulfide oxidation (e.g. when Mn is a component of pyrite), and/or from reactions with adjacent minerals (e.g., clays and carbonates) as the CMD is transported from its source to its surface discharge. In a survey of 140 abandoned coal mine discharges in Pennsylvania, the median Mn concentration was 2.35 mg/L with a range from 0.019 to 74.0 mg/L (Cravotta, 2008). Most of these discharges were from underground mines. For the surface coal mine at Site 1, the exceptionally high Mn

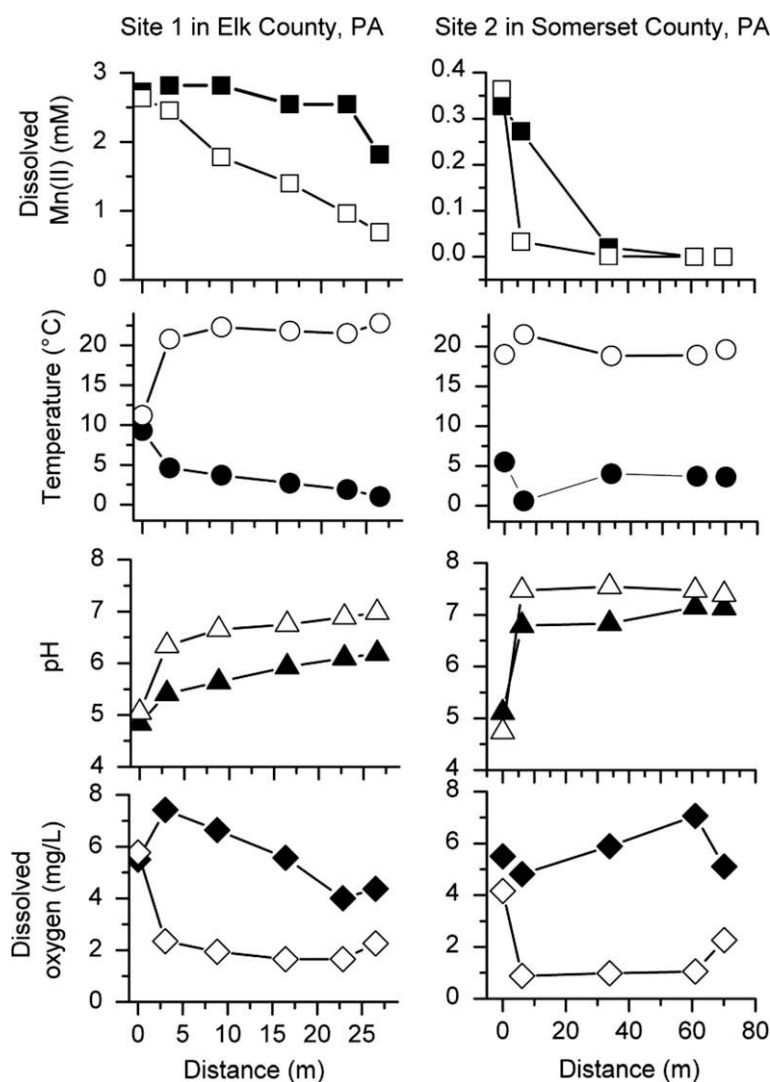**Fig. 1.** Seasonal water chemistry of Sites 1 and 2. Open symbols represent warm season (April 2006 for Site 1, July 2006 for Site 2) and filled symbols represent cold season (December 2005 for Site 1, February 2006 for Site 2). At Site 1, the six sampling points correspond to the influent pipe and five aeration ditches. At Site 2, the five sampling points correspond to the influent pipe, a test pit, and three piezometers.
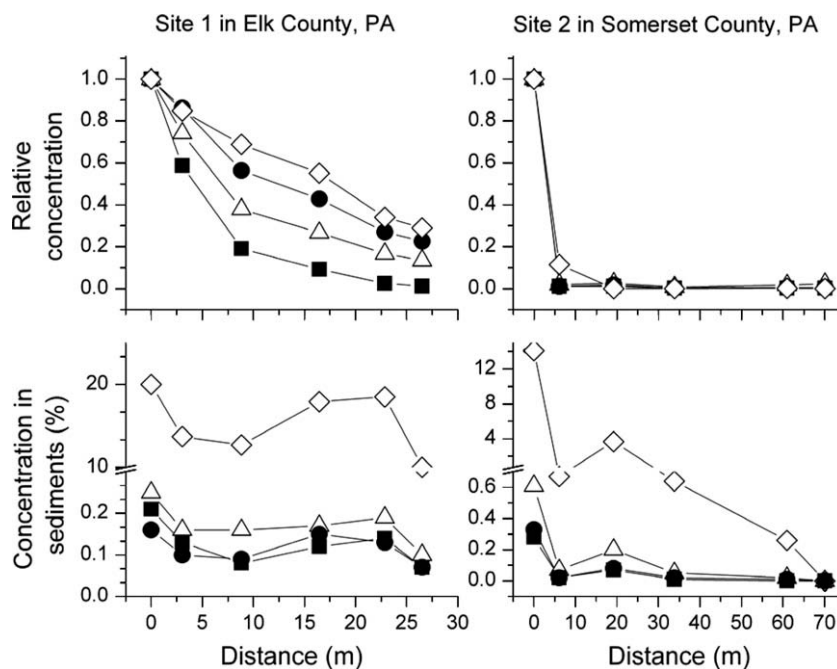
Fig. 2. Trace metal concentrations in water (top panels) and sediments (bottom panels) from Sites 1 and 2. Metal concentrations in water are normalized to their respective influent concentrations (absolute values reported in Table 2). Concentrations in sediments were reported as percentage of metal oxides in total sediments on a dry weight basis. Symbols: $\diamond$ (Mn), ● (Ni), $\triangle$ (Zn), ■ (Co).

concentration (130–150 mg/L) is believed to originate from reactions with the overburden. In a relevant study on Mn content in overburden from a coal strip mine in Tennessee, it was reported that Mn in siderite concretions was the most significant source while exchangeable Mn on clay minerals was a minor secondary source (Larsen and Mann, 2005). For comparison, the EPA secondary maximum contaminant limit for Mn in drinking water is 0.05 mg/L and the NPDES discharge limit for active coal mines is 4.0 mg/L.

The performance of these limestone Mn-removal beds were measured on several occasions between December 2005 and May 2007 to capture seasonal effects and other variability (Table 2). Representative data for Sites 1 and 2 for "warm" and "cold" months are presented in Fig. 1. The influent water temperature at Site 1 was relatively constant because the water emerged from an underground limestone drain. The influent water temperature at Site 2, like water temperature in both limestone beds, was strongly dependent on seasonal surface temperatures. Dissolved O_2 (DO) was strongly dependent on water temperature with higher DO in winter and lower DO in summer. Lower DO in summer could also have been caused by increased microbial activity in the beds, likely stimulated by increased productivity of upstream wetlands. The pH in the bed increased more slowly at Site 1 as compared to Site 2, probably because of the higher influent acidity.

Dissolved Mn(II) was never completely removed at Site 1, although greater removal occurred during warm months, suggesting biological activity may control Mn removal. Dissolved Mn(II) was removed to <0.05 mg/L before discharge from the bed at Site 2 for all sampling events. Enhanced Mn(II) removal (on *a*% basis) at Site 2 may have been caused by a combination of the lower influent Mn(II) load, the activity of microorganisms previously inoculated into the bed, and the higher pH in the bed. It has been demonstrated that Mn(II) oxidation occurs by both biological processes and by abiotic heterogeneous reactions with MnO_x surfaces in these beds (Tan, in preparation). The rate of abiotic Mn(II) oxidation has been shown to increase with increasing pH (Brewer, 1975; Davies and Morgan, 1989) such that this process could have been enhanced at Site 2. The rate of biological Mn(II) oxidation by *Lep-*

tothrix discophora SS1 has been shown to increase significantly between pH 6.0 to 7.5 (Zhang et al., 2002) such that this process could also have been enhanced at Site 2. The performance of the sandstone bed at Site 3 was monitored on only one occasion (May 2007) when the Mn(II) concentration decreased from 27 to 12 mg/L across the sandstone barrier.

The speciation of aqueous Mn(II) and the saturation indices (SI) for several Mn minerals were modeled for Site 1 using PHREEQC (Parkhurst and Appelo, 1999). These calculations were performed based on water chemistry measurements from the influent and all of the ditches across the treatment bed for a representative sampling event. Manganese^{2+} and $MnSO_4$ were the dominant aqueous species of Mn(II) based on these speciation calculations. At the influent end of the bed where the Mn(II) concentration was highest (1.58 mM), Mn^{2+} and $MnSO_4$ accounted for 63% and 37% of Mn(II)$_T$, respectively. At the effluent end of the bed where the Mn(II) concentration had decreased to 0.41 mM but the SO_4^{2-} concentration had remained constant (21 mM), Mn^{2+} and $MnSO_4$ accounted for 60% and 40% of Mn(II)$_T$, respectively. Equilibrium calculations also indicated that the ion activity products for species involved in the precipitation of birnessite, todorokite, hausmannite, bixbyite, pyrolusite, γ-MnO_2, manganite and $Mn(OH)_3$ exceed the solubility products of these minerals, suggesting that precipitation of Mn oxides was thermodynamically favorable. Manganese also exceeded the solubility of rhodochrosite ($MnCO_3$) although this mineral was not detected by XRD or Mn-EXAFS spectroscopy.

Additional water chemistry parameters were measured, on a less frequent basis, to examine nutrient status. At Site 1, concentrations of total organic C (TOC) downstream of the wetland were 4.3 mg C/L in December 2005 and increased to 8.4 mg C/L in April 2006. For one sampling event (September 2006), TOC ranged from 1.0 to 13 mg C/L across the bed, total N ranged from 0.07 to 0.46 mg N/L, and total P was less than 0.04 mg PO_4^{3-}/L. At Site 2, influent TOC concentrations downstream of the wetland were 8.9 mg C/L in February 2006 and increased to 28 mg C/L in July 2006. For one sampling event (May 2007), total N at Site 2 ranged from 0.07 to 0.24 mg N/L.

Table 3
Concentrations of major elements in sediments measured by ICP-AES following lithium metaborate fusion. Values are in oxide forms.

Concentration (%)	Site 1 inlet	Site 1 outlet	Site 2 inlet	Site 2 outlet
MnO_2	13.7	10.0	14.1	0.3
Al_2O_3	10.9	7.68	21.1	4.58
BaO	0.03	0.03	0.02	0.03
CaO	18.1	20.5	4.30	11.2
CuO	0.01	0.01	0.01	0
Fe_2O_3	1.56	1.95	1.40	2.64
K_2O	0.76	0.86	0.42	0.76
MgO	1.21	1.12	2.21	3.83
Na_2O	<0.05	<0.05	<0.05	<0.05
P_2O_5	0.12	0.27	0.05	0.18
SiO_2	23.9	29.4	11.3	12.3
SO_3	0.84	0.51	3.71	1.05
SrO	0.04	0.05	0.02	0.04
TiO_2	0.34	0.43	0.10	0.22
LOI (900 °C)	26.6	26.3	37.3	34.3

3.2. Trace metal chemistry

Trace metals are also of concern in CMD. In a survey of 140 abandoned coal mine discharges in Pennsylvania, the most abundant trace metals, in order of median concentrations (in µg/L), were Zn (140), Ni (85), Co (58), Ti (5.8), Cu (2.0), Cr (1.2), Pb (0.20) and Cd (0.12) (Cravotta, 2008). Elevated trace metals were found in both water and sediment samples at Sites 1 and 2 (Fig. 2, Table 2). The relative concentration trends of Zn > Ni > Co were found in both of these discharges, however, the influent concentrations of all metals were significantly higher than the median values reported by Cravotta (2008). Dissolved metal concentrations versus distance through the limestone beds were normalized to their respective influent concentrations in order to demonstrate preferential removal of trace metals versus Mn (Fig. 2). At Site 1, all trace metals were removed preferentially compared to Mn(II) and the order of preferential removal was Co > Zn > Ni > Mn(II). At Site 2, all dissolved trace metals were essentially removed within the first 5 m of the bed, and all to lower normalized concentrations compared to Mn(II). This selective uptake of trace metals into Mn oxides is consistent with several other studies on trace metal interactions with MnO_x (Fuller and Harvey, 2000; Kay et al., 2001; Tani et al., 2004).

Kay et al. (2001) and Tani et al. (2004) used sequential extraction techniques to investigate the mechanisms of trace metal removal by MnO_x. Their results indicated that Co can be removed by both sorption onto the MnO_x surface and by co-precipitation into the MnO_x structure. X-ray spectroscopy studies have shown that Co(II) can be oxidized after adsorption onto the MnO_x surface by either oxide-bound Mn(IV), oxide-bound Mn(III) or O_2, and further incorporated into the MnO_x structure (Manceau and Charlet,
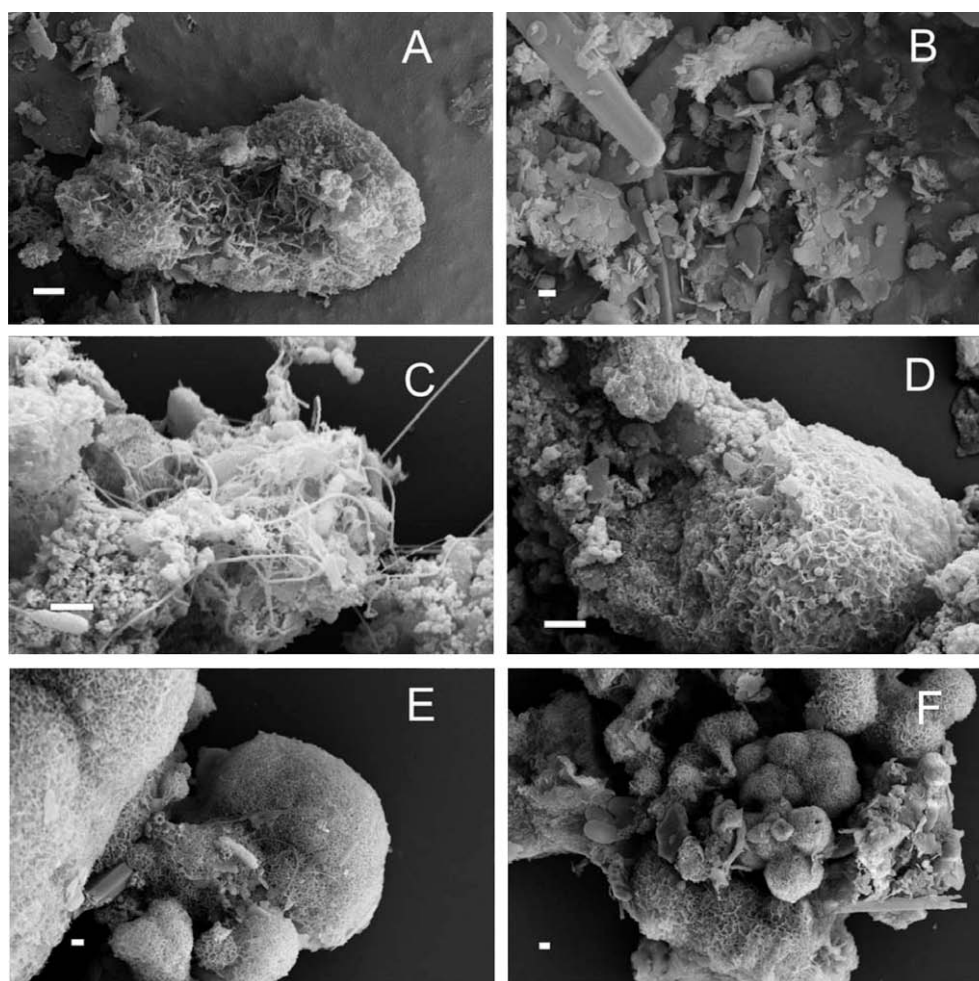
Fig. 3. Scanning electron micrographs of MnO_x-rich sediments collected from the 3 Mn(II)-removal systems. (A) Typical "sponge-like" morphology of the MnO_x crusts (Site 1, ditch 2). (B) Bacterial cells of various shape and freshwater diatoms shown in close proximity to MnO_x particles (Site 1, ditch 5). (C) Fungal mycelium shown in close proximity to MnO_x particles from Site 2. (D) "Sponge-like" morphology of the MnO_x crusts from Site 2. (E and F) MnO_x crusts from Site 3 where sandstone was used as a surface to precipitate Mn(II). Scale bar in all images represents 1 µm.

1992; Manceau et al., 1992, 1997). In contrast, Ni is not readily oxidized and the extent of Ni substitution into the MnO_x structure is limited (Hem et al., 1989; Manceau et al., 1987). Kay et al. (2001) found that Ni competes with Mn(II) for sorption sites and Ni sorption is highly reversible. Toner et al. (2006) investigated Zn sorption onto biogenic hexagonal birnessite using EXAFS spectroscopy and concluded that Zn preferentially partitioned into the interlayer of birnessite and formed a chalcophanite-like structure.

MnO_x-rich sediment crusts were collected from the same locations as the water samples, dissolved following Li metaborate fusion and analyzed for elemental composition (Fig. 2, Table 3). Preferential removal of trace metals was not as apparent based on trends of sediment concentrations, however, metal accumulation in sediments represents a much longer (and potentially variable) time-composited sampling period. Equilibrium speciation calculations indicated that waters containing the corresponding dissolved concentrations of Co, Ni and Zn were undersaturated with respect to corresponding metal carbonates and hydroxides at both Sites 1 and 2. The one exception was at Site 1, where equilibrium calculations predicted that waters containing Co, Ni and Zn were slightly oversaturated with respect to some silicate minerals.

3.3. Mineralogy of Mn precipitates

The basic building block of MnO_x minerals is octahedrally coordinated Mn, which can assemble into three major structural groups: chains (e.g. pyrolusite), tunnels (e.g. todorokite), and layers (e.g. birnessite and "buserite"). Chain structures consist of edge-sharing octahedra, tunnel structures are formed when multiple chains share corners to produce square or rectangular cross sections, and layer structures consist of stacked sheets of edge-sharing octahedra (Post, 1999). Birnessite and buserite (not an official mineral name) have similar layer structures and have been identified as important forms of biogenic MnO_x (Webb et al., 2005a). Birnessites are fine-grained and relatively poorly crystalline with an interlayer spacing of 7 Å that incorporates cations and water molecules. Buserite has a 10 Å interlayer spacing and contains an extra water layer that is lost upon drying causing the structure to collapse to a 7 Å interlayer spacing. This dehydration process is irreversible and often used to distinguish between buserite and todorokite, which also has a 10 Å interlayer spacing but is stable upon drying (Post, 1999). However, some cations such as Ca, Mg, Ni and Cu can stabilize the 10 Å spacing in the buserite structure from collapse upon drying (Tebo et al., 1997).

At Site 1, thick, black-grey MnO_x coatings were observed in every ditch in the limestone bed. In test pits dug into the bed at Site 1, MnO_x coatings did not extend very deeply beyond the air–water interface. Similarly, in test pits dug into the bed at Site 2, black MnO_x precipitates were found to accumulate at the air–water interface and decrease with depth. At Site 3, exceptionally thick, black MnO_x precipitates covered the exposed sandstone surfaces. Compared to the MnO_x precipitates found in the limestone beds, precipitates on the sandstone bed appeared darker with less clay content and debris.

Based on SEM images, samples from all three sites showed similar surface morphologies regardless of influent Mn(II) concentrations, ±inoculation with patented Mn(II)OB, or bed materials (limestone vs. sandstone). An extremely coarse, "sponge-like" texture of the MnO_x precipitates were commonly observed in samples from all three sites (Fig. 3). Biological features that resembled bacterial cells, freshwater diatoms and fungal mycelia were also observed in samples from all three sites. The intimate proximity of both prokaryotic and eukaryotic organisms to the MnO_x precipitates suggests that biological oxidation likely led to MnO_x formation. Inorganic materials such as clay particles and limestone and sandstone fragments were also observed in samples from all three

sites. It was possible to isolate and examine just the MnO_x precipitates using whole mount high resolution TEM (Fig. 4). The coarse morphology observed in SEM images was consistent with TEM images of the MnO_x precipitates which revealed fibrous nm-sized lathes and thin sheets. Elemental analysis by EDS confirmed that this material was a Mn oxide with trace amounts of Ca and Al. SAED rings demonstrated that this material was relatively amorphous and non-crystalline.

XRD and SR-XRD patterns also established that the MnO_x precipitates collected from these systems were relatively amorphous and non-crystalline (Fig. 5). Identification of the specific MnO_x minerals was operationally defined based on the presence/absence of a specific diffraction peak from wet and oven-dried samples.
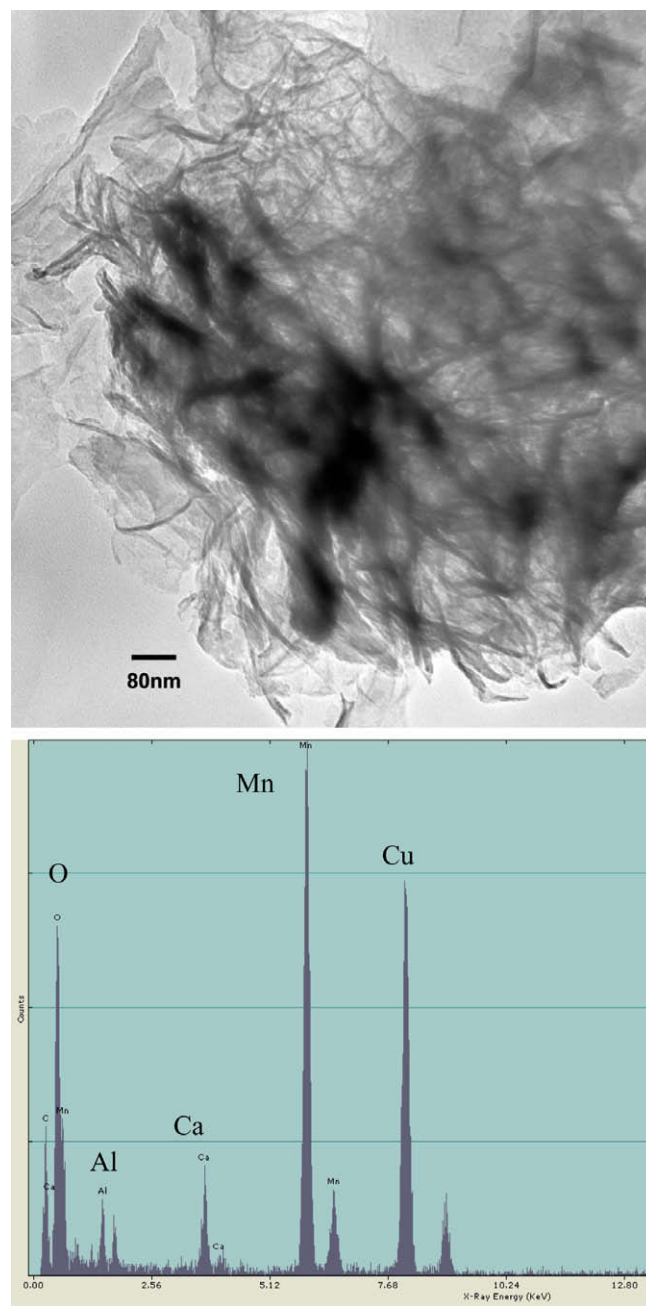

Fig. 4. Transmission electron micrograph of MnO_x particles collected from Site 1. Elemental analysis in lower panel obtained from energy dispersive spectroscopy from most electron-dense portion of upper panel (Cu signal comes from TEM Cu grid).

XRD patterns from all samples from all sites showed strong peaks at 10 Å d-spacing. Several synthetic and natural Mn oxides have 10 Å d-spacings, including todorokite and buserite (Post, 1999; Bilinski et al., 2002). For Site 1, XRD patterns showed the sample contained calcite, quartz and a 10 Å Mn oxide. The wet sample had a strong peak at 10 Å and a very weak peak at 7.0 Å. After drying, the 10 Å peak diminished and the 7.0 Å peak became more significant which suggests that this sample contained mostly buserite. For Site 2, XRD patterns showed the sample contained quartz, dolomite, and a 10 Å Mn oxide. The wet sample had a strong peak at 10 Å and a very weak peak at 7.0 Å. After drying, the 10 Å peak did not disappear nor did the 7.0 Å peak increase which suggests the MnO_x in this sample could be todorokite or buserite with cations incorporated into the interlayer (helps resist collapse upon drying) (Fig. 5). The MnO_x from Site 3 had an additional, uncharacteristic, very broad peak at ~8.5 Å that could be a result of the partial loss of water from the birnessite interlayer (Fig. 6).

Manganese-EXAFS spectroscopy was used to further characterize these samples (Fig. 7) and quantify the relative distribution of MnO_x minerals. Using an assemblage of three presumed MnO_x mineral standards; hexagonal birnessite, triclinic birnessite and todorokite, linear combination fitting (LCF) of the EXAFS spectra was used to calculate the relative distribution of these minerals (Table 4). The predominant MnO_x minerals at all sites were hexagonal birnessite and triclinic birnessite. Todorokite was found to account for 14–29% of the MnO_x minerals at Site 1, 0–5% of the MnO_x minerals at Site 2, and 2% of the MnO_x minerals at Site 3. At Site 3, the MnO_x was essentially pure hexagonal birnessite. Manganese

EXAFS spectroscopy compliments XRD results and further clarifies the phases presents in these samples. At Site 1, the presence of todokorite and birnessite is consistent with similar findings from cemented MnO_x crusts collected at Pinal Creek, Arizona (Bilinski et al., 2002). The transformation of buserite to todokorite can occur under atmospheric conditions in laboratory experiments, and this process is affected by temperature, pH and the addition of pyrophosphate (a Mn(III) complexant) (Cui et al., 2006, 2008). Bilinski et al. (2002) postulated that todorokite and birnessite at Pinal Creek were transformed from buserite under different conditions. This could explain differences in MnO_x mineral assemblages at Site 1 (i.e. ditch 1 vs. ditch 4) promoted by changes in water chemistry through the limestone bed.

For Site 2, XRD showed that the 10 Å MnO_x mineral could be todorokite or cation-stabilized buserite while EXAFS spectroscopy showed relatively low (0–5%) todorokite content. Discerning todorokite and cation-stabilized buserite by XRD alone can be difficult (Arrhenius and Tsai, 1981; Giovanoli and Arrhenius, 1988). Mandernack et al. (1995) showed that Ca and Mg can stabilize the structure of buserite from collapsing at room temperature, but this effect at higher temperatures is not clear. For Site 3, XRD showed a relatively amorphous MnO_x mineral while EXAFS spectroscopy identified the mineral assemblage as nearly 100% hexagonal birnessite. The relatively simple MnO_x mineralogy at Site 3 could be due to differences in influent water chemistry compared to Sites 1 and 2 (Table 2). In particular, the alkaline pH and lower concentrations of Al and other trace metals could favor the formation of a more relatively "pure" MnO_x precipitate. The relatively simple MnO_x mineralogy at Site 3 could also be due to faster kinetics of
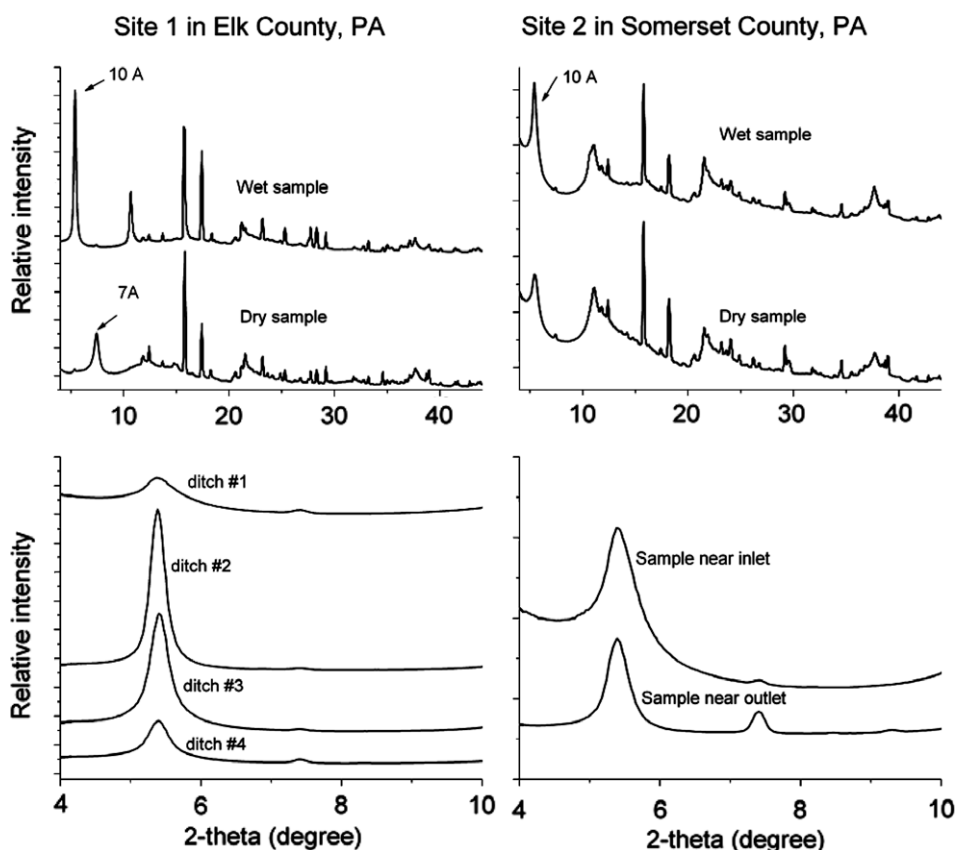

Fig. 5. Synchrotron radiation X-ray diffraction patterns from MnO_x-rich sediments collected from Site 1 (L panels) and Site 2 (R panels). Upper panels present stacked comparisons of wet samples vs. 110 °C oven-dried samples. Upper L sample collected from Site 1 (ditch 2), and upper R panel collected from Site 2 (near inlet). Lower panels present stacked comparisons of pattern details in the low 2-theta region for a series of wet samples. The 10 Å peaks were used to calculate crystallite size based on full width half maximum (FWHM). Wavelength of the synchrotron radiation was 0.91594 Å.
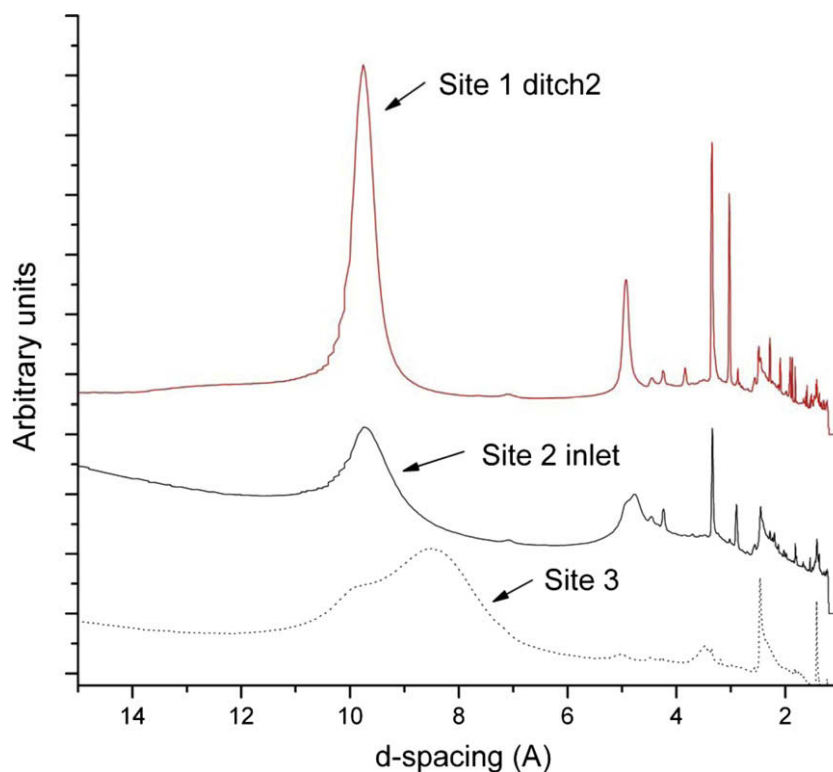
Fig. 6. Comparison of synchrotron radiation X-ray diffraction patterns from moist MnO_x-rich sediments collected from all three sites. Wavelength of the synchrotron radiation was 0.97516 Å.
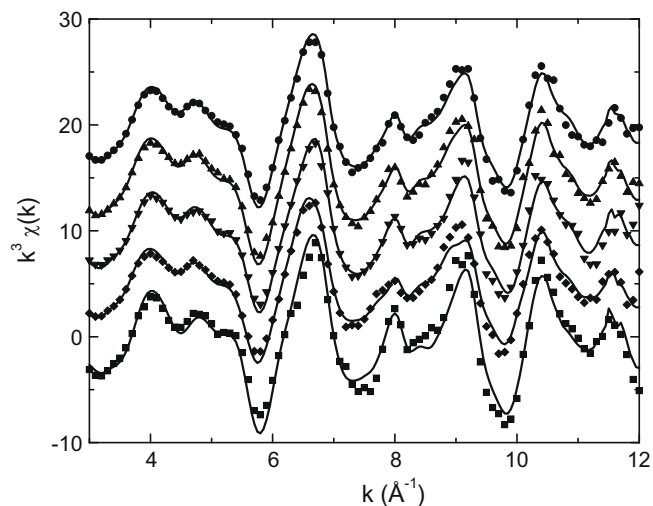

Fig. 7. Manganese K-edge EXAFS spectra from natural MnO_x-rich sediments collected from the three Mn(II)-removal systems. The measured spectra (symbols) are shown with model fits (lines). Spectra were fit as a linear combination of hexagonal birnessite, triclinic birnessite, and todorokite. Results of the fits are included in Table 4. The samples shown were collected from (top to bottom): A – Site 1 ditch 1 (circle); B – Site 1 ditch 5 (up triangle); C – Site 2 influent trench (down triangle); D – Site 2 effluent stream (diamond); and, E – Site 3 barrier (square).

Table 4
Results from linear combination fitting (LCF) of Mn K-edge EXAFS spectra from MnO_x-rich sediments collected from the three Mn(II)-removal systems. Mn K-edge EXAFS spectra are shown in Fig. 7.

Site number, sample name	% Hexagonal birnessite	% Triclinic birnessite	% Todorokite
Site 1, ditch 2	59	12	29
Site 1, ditch 4	62	24	14
Site 2, influent trench	65	35	0
Site 2, effluent stream	45	50	5
Site 3, barrier	98	2	0

decrease from 27 to 12 mg/L across the barrier in just a few minutes residence time.

3.4. Environmental implications

The "active" removal of Mn(II) from CMD is considerably more expensive than "passive" removal in limestone beds. The Mn oxides formed in these passive treatment systems are themselves extremely important in the further removal of Mn(II) and trace metals from CMD. In this study it was found that MnO_x formed in CMD treatment systems were primarily poorly crystalline layered buserite of small particle size and coarse texture, which scavenged trace metals such as Co, Ni and Zn. In one of the CMD treatment systems (Site 1), trace metals were preferentially removed likely via co-precipitation with Mn oxides. The crystallite sizes of MnO_x minerals formed in the ditches in Site 1 were calculated using Scherrer's equation based on the full-width half-maximum (FWHM) of the 10 Å peak. The crystallite size was shown to be smallest at the influent end of the bed (5.0 nm) where more trace metal incorporation could have occurred.

Mn(II) oxidation and precipitation. Both high pH and high DO promote more rapid biotic (Zhang et al., 2002) and abiotic Mn(II) oxidation (Davies and Morgan, 1989). Alkaline water breaching the sandstone barrier was well aerated providing both of these conditions and helps explain how the Mn(II) concentration could

The assemblage of MnO_x minerals identified by XRD (Figs. 5 and 6) and quantified by LCF of the Mn-EXAFS spectra (Table 4 and Fig. 7) were relatively similar for the two biologically active Mn-removal beds (Sites 1 and 2). The findings suggest buserite and todorokite may be common products in CMD treatment systems despite differences in construction, microbial community structures, nutrients sources, and influent water chemistry. However, the MnO_x identified at Site 3 was essentially pure hexagonal birnessite. At Site 3 it is believed that Mn(II) precipitation was promoted by the alkaline, aerated water chemistry and by the catalytic effects of the MnO_x/sandstone surfaces during the relatively short residence time across the sandstone barrier.

Acknowledgments

References

Arrhenius, G., Tsai, A.G., 1981. Structure, phase transformation and prebiotic catalysis in marine manganate minerals. SIO Ref. Ser. 81–28, 1–19.

Bargar, J.R., Tebo, B.M., Villinski, J.E., 2000. In situ characterization of Mn(II) oxidation by spores of the marine *Bacillus* sp. strain SG-1. Geochim. Cosmochim. Acta 64, 2775–2778.

Bargar, J.R., Tebo, B.M., Bergmann, U., Webb, S.W., Glatzel, P., 2005. Biotic and abiotic products of Mn(II) oxidation by spores of the marine *Bacillus* sp. strain SG-1. Am. Miner. 90, 143–154.

Bilinski, H., Giovanoli, R., Usui, A., Hanzel, D., 2002. Characterization of Mn oxides in cemented streambed crusts from Pinal Creek, Arizona, USA, and in hot-spring deposits from Yuno-Taki Falls, Hokkaido, Japan. Am. Mineral. 87, 580–591.

Brewer, P.G., 1975. Minor elements in sea water. In: Riley, J.P., Skirrow, G. (Eds.), Chemical Oceanography. Academic Press, pp. 415–496.

Cravotta, C.A., 2008. Dissolved metals and associated constituents in abandoned coal-mine discharges, Pennsylvania, USA. Part 2: geochemical controls on constituent concentrations. Appl. Geochem. 23, 203–226.

Cui, H.J., Feng, X.H., He, J.Z., Tan, W.F., Liu, F., 2006. Effects of reaction conditions on the formation of todorokite at atmospheric pressure. Clay Clay Miner. 54, 605–615.

Cui, H.J., Liu, X., Tan, W., Feng, X., Liu, F., Ruan, H.D., 2008. Influence of Mn(III) availability on the phase transformation from layered buserite to tunnel-structured todorokite. Clay Clay Miner. 56, 397–403.

Davies, S.H.R., Morgan, J.J., 1989. Manganese(II) oxidation kinetics on metal oxide surfaces. J. Colloid Interface Sci. 129, 63–77.

Fuller, C., Harvey, J., 2000. Reactive update of trace metals in the hyporheic zone of mining-contaminated stream, Pinal Creek, Arizona. Environ. Sci. Technol. 34, 1150–1155.

Ghiorse, W.C., 1984. Biology of iron- and manganese-depositing bacteria. Ann. Rev. Microbiol. 38, 515–550.

Giovanoli, R., Arrhenius, G., 1988. Structural chemistry of marine manganese and iron minerals and synthetic model compounds. In: Halbach, P., Friedrich, G., von Stackelberg, U. (Eds.), The Manganese Nodule Belt of the Pacific Ocean; Geological Environment, Nodule Formation, and Mining Aspects. Ferdinand Enke Verlag, Berlin, pp. 20–37.

Goto, K., Taguchi, S., Fukue, Y., Ohta, K., Watanabe, H., 1977. Spectrophotometric determination of manganese with 1-(2-pyridylazo)-2-naphthol and a non-ionic surfactant. Talanta 24, 752–753.

Hansel, C.M., Francis, C.A., 2006. Coupled photochemical and enzymatic Mn(II) oxidation pathways of a planktonic *Roseobacter*-like bacterium. Appl. Environ. Microbiol. 72, 3543–3549.

Hem, J., Lind, C., Roberson, C., 1989. Coprecipitation and redox reactions of manganese oxides with copper and nickel. Geochim. Cosmochim. Acta 53, 2811–2822.

Hungate, B., Danin, A., Pellerin, N.B., Stemmler, J., Kjellander, P., Adams, J.B., Staley, J.T., 1987. Characterization of manganese-oxidizing (MnII → MnIV) bacteria from Negev Desert rock varnish: implications in desert varnish formation. Can. J. Microbiol. 33, 939–943.

Jenne, E.A., 1968. Controls on Mn, Fe, Co, Ni, Cu, and Zn concentrations in soils and water: the significant role of hydrous Mn and Fe oxides. Adv Chem Ser, 337–387.

Johnson, K.L., Younger, P.L., 2005. Rapid manganese removal from mine waters using an aerated packed-bed bioreactor. J. Environ. Qual. 34, 987–993.

Junta, J.L., Hochella, M.F., 1994. Manganese (II) oxidation at mineral surfaces: a microscopic and spectroscopic study. Geochim. Cosmochim. Acta 58, 4985–4999.

Katsoyiannis, I.A., Zouboulis, A.I., Jekel, M., 2004. Kinetics of bacterial As(III) oxidation and subsequent As(V) removal by sorption onto biogenic manganese oxides during groundwater treatment. Ind. Eng. Chem. Res. 43, 486–493.

Kay, J., Conklin, M.H., Fuller, C., O'Day, P.A., 2001. Processes of nickel and cobalt uptake by a manganese oxide forming sediment in Pinal Creek, Globe Mining District, Arizona. Environ. Sci. Technol. 35, 4719–4725.

Larsen, D., Mann, R., 2005. Origin of high manganese concentrations in coal mine drainage, eastern Tennessee. J. Geochem. Explor. 86, 143–163.

Lopano, C.L., Heaney, P.J., Post, J.E., Hanson, J., Komarneni, S., 2007. Time-resolved structural analysis of K- and Ba-exchange reactions with synthetic Na-birnessite using synchrotron X-ray diffraction. Am. Mineral. 92, 380–387.

Manceau, A., Charlet, L., 1992. X-ray absorption spectroscopy study of the sorption of Cr(III) at the oxide water interface. J. Colloid Interface Sci. 148, 425–442.

Manceau, A., Llorca, S., Calas, G., 1987. Crystal-chemistry of cobalt and nickel in lithiophorite and asbolane from new-caledonia. Geochim. Cosmochim. Acta 51, 105–113.

Manceau, A., Gorshkov, A., Drits, V., 1992. Structural chemistry of Mn, Fe, Co, and Ni in manganese hydrous oxides. 2. Information from EXAFS spectroscopy and electroscopy and X-ray diffraction. Am. Miner. 77, 1144–1157.

Manceau, A., Drits, V., Silvester, E., Bartoli, C., Lanson, B., 1997. Structural mechanism of CO^{2+} oxidation by the phyllomanganate buserite. Am. Mineral. 82, 1150–1175.

Mandernack, K.W., Post, J., Tebo, B.M., 1995. Manganese mineral formation by bacterial-spores of the marine *bacillus*, strain Sg-1 – evidence for the direct oxidation of Mn(II) to Mn(IV). Geochim. Cosmochim. Acta 59, 4393–4408.

Means, B., Hilton, T., 2004. Comparison of three methods to measure acidity of coal-mine drainage. In: Proc. Natl. Meeting American Society of Mining and Reclamation and 25th West Virginia Surface Mine Drainage Task Force. American Society of Mining and Reclamation, Lexington, KY, pp. 1249–1277.

Means, B., Rose, A.W., 2005. Rate of manganese removal in limestone bed systems. In: Proc. Ann. Meeting. American Society of Mining and Reclamation, Breckenridge, CO, pp. 702–716.

Mouchet, P., 1992. From conventional to biological removal of iron and manganese in France. J. Am. Water Works Assoc. 84, 158–167.

Nealson, K.H., Tebo, B.M., Rosson, R.A., 1988. Occurrence and mechanisms of microbial oxidation of manganese. Adv. Appl. Microbiol. 33, 279–318.

Parkhurst, D.L., Appelo, C.A.J., 1999. User's guide to PHREEQC (version 2) – a computer program for speciation, batch-reaction, one-dimensional transport, and inverse geochemical calculations. US Geol. Surv. Water-Resour. Invest. Rep., 99–4259.

Post, J.E., 1999. Manganese oxide minerals: crystal structures and economic and environmental significance. Proc. Natl. Acad. Sci. 96, 3447–3454.

Rehr, J.J., Albers, R.C., Zabinsky, S.I., 1992. High-order multiple-scattering calculations of X-ray-absorption fine structure. Phys. Rev. Lett. 69, 3397–3400.

Sikora, F.J., Behrends, L.L., Brodie, G.A., Taylor, H.N., 2000. Design criteria and required chemistry for removing manganese in acid mine drainage using subsurface flow wetlands. Water Environ. Res. 72, 536–544.

Stone, A., 1987. Reductive dissolution of manganese(III/IV) oxides by substituted phenols. Environ. Sci. Technol. 21, 979–988.

Tan, H.T., in preparation. Microbial communities and manganese mineralogy associated with manganese(II)-removal systems for coal mine drainage. Ph.D. Dissertation. The Pennsylvania State Univ.

Tani, Y., Ohashi, M., Miyata, N., Seyama, H., Iwahori, K., Soma, M., 2004. Sorption of Co(II), Ni(II), and Zn(II) on biogenic manganese oxides produced by a Mn-oxidizing fungus, strain KR21-2. J. Environ. Sci. Health A 39, 2641–2660.

Tebo, B.M., 1991. Manganese(II) oxidation in the suboxic zone of the Black Sea. Deep-Sea Res. 38, S883–S905.

Tebo, B.M., Ghiorse, W.C., van Waasbergen, L.G., Siering, P.L., Caspi, R., 1997. Bacterially mediated mineral formation: insights into manganese(II) oxidation from molecular genetic and biochemical studies. In: Banfield, J.F., Nealson, K.H. (Eds.), Geomicrobiology: Interactions Between Microbes and Minerals. Reviews in Mineralogy 35, 225–266.

Tebo, B.M., Bargar, J.R., Clement, B.G., Dick, G.J., Murray, K.J., Parker, D., Verity, R., Webb, S.M., 2004. Biogenic manganese oxides: properties and mechanisms of formation. Ann. Rev. Earth Planet. Sci. 32, 287–328.

Templeton, A.S., Staudigel, H., Tebo, B.M., 2005. Diverse Mn(II)-oxidizing bacteria isolated from submarine basalts at Loihi Seamount. Geomicrobiol. J. 22, 127–139.

Thompson, I.A., Huber, D.M., Guest, C.A., Schulze, D.G., 2005. Fungal manganese oxidation in a reduced soil. Environ. Microbiol. 7, 1480–1487.

Thornton, F.C., 1995. Manganese removal from water using limestone-filled tanks. Ecol. Eng. 4, 11–18.

Toner, B., Manceau, A., Webb, S.M., Sposito, G., 2006. Zinc sorption to biogenic hexagonal-birnessite particles within a hydrated bacterial biofilm. Geochim. Cosmochim. Acta 70, 27–43.

Vail, W.J., Riley, R.K., 2000. The pyrolusite process: a bioremediation process for the abatements of acid mine drainage. Green Lands 30, 40–46.

Villalobos, M., Toner, B., Bargar, J.R., Sposito, G., 2003. Characterization of the manganese oxide produced by pseudomonas putida strain MnB1. Geochim. Cosmochim. Acta 67, 2649–2662.

Webb, S.M., Tebo, B.M., Bargar, J.R., 2005a. Structural characterization of biogenic Mn oxides produced in seawater by the marine *bacillus* sp. strain SG-1. Am. Mineral. 90, 1342–1357.

Webb, S.M., Tebo, B.M., Bargar, J.R., 2005b. Structural influences of sodium and calcium ions on the biogenic manganese oxides produced by the marine *bacillus* sp., strain SG-1. Geomicrobiol. J. 22, 181–193.

Zhang, J.H., Lion, L.W., Nelson, Y.M., Shuler, M.L., Ghiorse, W.C., 2002. Kinetics of Mn(II) oxidation by *Leptothrix discophora* SS1. Geochim. Cosmochim. Acta 66, 773–781.